



Report on the terahertz computed tomography (THz-CT) technique in comparison to X-rays computed tomography (XCT)

Deliverable D1
Lead author: CNRS

Project 15HLT09 “MetAMMI Metrology for additively manufactured medical implants”.

Due date: 31st May 2019
Submission date: 5rd June 2019





Content

1.	<i>Presentation of computed tomography (CT)</i>	3
1.1.	THz imaging	3
1.2.	Time of flight (TOF) imaging	5
1.3.	THz Computed tomography (THz-CT)	5
2.	<i>Data Processing and reconstruction</i>	6
2.1.	Direct methods	6
2.2.	From the physical phenomenon to the reconstruction	7
2.3.	Acquisition properties	8
3.	<i>THz imaging in MetAMMI context</i>	8
3.1.	Terahertz and X-ray reports: Two beams, two worlds	9
3.2.	Introduction to acceptance testing	10
3.3.	Experimental setups	11
3.3.1.	X-ray CT scans	11
3.3.2.	THz-CT scans	12
3.4.	Data Evaluation	13
3.4.1.	Dimensional and geometrical analyses	16
3.5.	Extraction of coordinates and diameters of circular openings on THz images	17
3.6.	2D measurement from the point by point imaging	17
3.7.	3D measurement from the imaging field	23
3.8.	Uncertainties on measuring the dimension of an object with THz waves	26
4.	<i>Advantages / limitations of THz and X-ray imaging</i>	27

1. Presentation of computed tomography (CT)

The word tomography is derived from the Greek word tomos meaning ‘slice’ or ‘section’ and graphia meaning ‘describing’. The field of tomography involves methods for obtaining cross sectional images of a target, allowing the internal details to be observed. Computed tomography (CT) is a technique that consists in reproducing the structure of an object by acquiring a series of projections all around the considered object using electromagnetic waves (microwaves, terahertz waves, X-ray, etc.) or elastic waves (sound, ultrasound, etc.).

In X-Ray CT, the propagation of the beam is considered to be straight and without diffraction because of the small wavelength. At the opposite, in terahertz (THz) CT, the beam shape is close to a Gaussian distribution due to the THz wave properties and to the lens used to enforce the beam focus (Fig. 1).

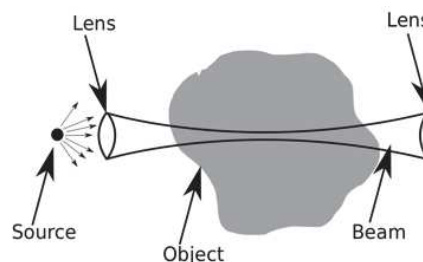


Figure 1: The schematic of THz-CT beam.

The projections are measured from the exterior of the object according to the Radon Transform (Fig. 2). Each projection value corresponds to the absorption sum along the ray which crosses the object.

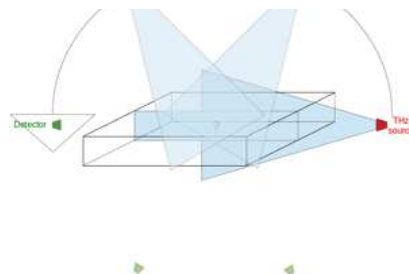


Figure 2: Procedure for the acquisition.

1.1. THz imaging

Electromagnetic (EM) spectrum contains several regions with different properties allowing specific developments and achievements in many application fields. Since the mid twentieth century, a particular region of the EM spectrum has been extensively studied, ranging between infrared and microwaves, and known as terahertz domain. In this domain, the frequencies of the EM waves are ranging between 0.1 and 30 THz ($1 \text{ THz} = 10^{12} \text{ Hz}$), which correspond to the wavelengths between 3 mm and 10 μm . THz waves share the characteristics of both infrared and microwaves domains, namely:

- Non-ionizing: photons in the THz region have low energies, ranging between 0.41 meV and 124 meV. This low energy has no ionizing effect on biological tissues.



- Chemical signature/fingerprints: solid, liquid or gas, several materials have their own signature after interaction with the THz waves, which allow their identification. This property is widely exploited in THz spectroscopy applications as for example the case of powders identification.
- High transmission/penetration in non-dielectric materials: many amorphous materials are transparent for THz waves, such as plastic, textile, paper, ceramic etc. This permits non-contact inspection applications and imaging.[1]
- Absorption of polar liquids such as water: this particularity highlights the potential of THz waves in specific applications. Also, being absorbed by water, THz waves cannot penetrate more than several dozen of micrometer through the skin for example.

One main limitation of the terahertz waves is that they are not able to pass through metal. But the combination of all the other characteristics mentioned before, provides the THz radiations with a high potential in many applications.

An X-ray beam is a flow of discrete photon particles, each having a specific energy. The attenuation of this photon with matter occurs via four basic modes of interaction: coherent X-ray scatter, incoherent or Compton scatter, photoelectric absorption and pair production

Terahertz technology has been making clear progress following recent advances in femtosecond lasers and ultrafast semiconductor coherent sources emitting in the THz frequency range [2]. However, the development of brighter sources and efficient detectors that are more sensitive to THz waves is a key feature to efficiently use these waves in THz spectroscopy [3]. Consequently they can be used to control, image or analyze samples through many types of packaging materials, including paper, plastics, leather, ceramic or wood and allow imaging in a standoff configuration [4]. Moreover, the interaction of matter with THz waves is non-invasive, and thus these radiations can also be used to probe fragile biological materials [5], for medical diagnostics or bio medical imaging [6] not only for basic research, but also for applications in a wide variety of fields.

Ranging between far infrared and microwaves, the development of terahertz science and technology [7] comes from both the electronics and optics sides. Recent innovations in terahertz technology take advantages from two outstanding ideas and concepts from each individual field. More recently, the inventory of applications has increased and includes quality control, non-destructive testing (NDT) [8] [9] and spectroscopic characterization of materials or chemical recognition [10]. Many of these applications rely on the exceptional features of terahertz radiation which consist in the transparency of common packaging materials and the fact that many interesting materials exhibit unique spectral fingerprints in the terahertz range. This huge advantage can be exploited in industrial applications [11], for identification and chemical analysis.

In recent years, a number of methods for 2D and 3D imaging with THz radiations have been proposed and demonstrated. Since the development of pulsed THz systems, such 3D imaging systems have been proposed [12]. Let's describe briefly the different physical techniques capable of extracting 2D and 3D information we used in the project. X-rays possess intrinsic energy that may be imparted to the matter they interact with. That interaction takes place as either absorption (transfer of energy from the X-ray photon to the absorbing material) or scattering (in which the X-ray photon is "redirected" by interaction with the scattering material). The process of scattering is the primary process responsible for diffraction, but both processes (that are, in many ways, interdependent) result in the production of potentially damaging secondary radiation. That radiation is capable of producing significant short- and long-term health effects in the event of exposure to human tissue. Therefore, appropriate radiation protection measures are necessary. For Terahertz interaction, frequency dispersion refers to the phenomenon in which waves of different frequencies propagate at different speeds. Dispersion, together with absorption, characterizes how media respond to external



electromagnetic fields. All electromagnetic phenomena involve the interaction of fields with charged particles, electrons and nuclei at a microscopic scale, in matter. Electromagnetic waves force charged particles to move; their accelerated motion induces radiation. The effects of magnetic fields on naturally occurring materials are mostly negligible and the amplitude of the electron motions are usually very small. Consequently, electromagnetic properties of a medium are dominated by electric dipoles induced by the applied electric fields. In the linear optical regime, the electric dipole moments are proportional to the amplitude of the applied electric fields.

1.2. Time of flight (TOF) imaging

THz pulsed imaging has the unique feature of providing a 3D image "map" of the object by using the time-of-flight of the reflected THz pulses [13]. Briefly, a THz pulse is directed on the target and the amplitude and timing (time-of-flight) of the reflected pulse are measured. The temporal position of the reflected pulses directly correlates with the location of the interfaces along the propagation direction of the beam. In this way, depth information of the 3D profiles of the target can be obtained by using the difference of time-of-flight, which is converted into the difference of the depth. Mittleman *et al* were the first to report on such 3D THz imaging [14]. The 3D image of a floppy disk was successfully reconstructed by using the reflected THz pulses via a digital signal processing algorithm. However, this early THz tomography tool was based on three assumptions:

- (1) Targets have no dispersion and diffraction,
- (2) Reflection is weak so that multi-reflection can be neglected or suppressed,
- (3) Refractive index is uniform within each layer.

1 & 3 are assumed with polymer materials which present low dispersion especially in the lower part of the THz frequency range.

In this technique, as the arrival time of the THz waveforms can be determined with an accuracy of a few femtoseconds, i.e. much less than the pulse duration, the position of reflecting surfaces within the test object, can be determined with an accuracy of a few micrometers, when successive reflections are well separated in time. A very high depth resolution (lateral resolution) in the order of 1 μm has been demonstrated [13].

The resolution depends on the width of the incident THz pulse, and is improved when the pulse is short. When the THz pulse is not ideal (e.g., a top-hat function), but varies with time in the same way, distinction of the reflected pulse becomes difficult, and ghost interfaces can appear in the tomographic image. These ghost images can be eliminated using signal processing, for example by employing deconvolution algorithms.

TOF tomography (use this technique to display 3D images) is well adapted for layered targets with well-defined boundaries. However, when the object has a more complicated structure (internal or external shape), the multiple reflections and refractions of the THz radiations are superposing and render the detection of the back-reflected signal indistinguishable. In such a case, the best solution is to perform a THz-CT analysis with a set of projection images. Moreover, a powerful new imaging modality for terahertz radiation has been proposed: THz-ray reflection computed tomography. In this method, edge maps of an object's cross-section are reconstructed from a series of time-domain reflection measurements at different viewing angles.

1.3. THz Computed tomography (THz-CT)

Computed tomography (CT) is an effective imaging method to visualize the internal structure of a three-dimensional (3D) object as cross-sectional images. In this method, a series of transmitted

images are measured at different projection angles and the internal structure of the object is reconstructed by analyzing these images with specific reconstruction algorithms, such as the filtered back-projection (FBP) algorithm using inverse Radon transform [15]. Conventionally, X-ray CT has been widely used in non-destructive testing, quality control, material characterization and biomedical imaging. However, the hazardous ionizing effects of X-ray and its costs limit its utility in industry.

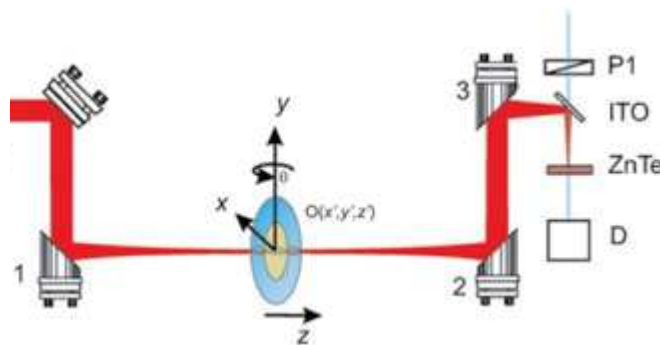


Figure 3: setup of THz-CT experiment

Recently, terahertz (THz) radiation has emerged as a new mode for CT owing to free-space propagation, low photon energy, moderate penetration through soft materials and broad spectral range. Since the first demonstration of THz-CT in 2002, THz-CT along with spectral analysis offers the opportunity of wide spectral information in the time and frequency domains, so one may reconstruct images at each frequency value. A typical experimental configuration is presented in fig 3. Brahm *et al.* also performed a volumetric spectral analysis of materials using THz-CT [16]. Based on their characteristic absorption spectrum, lactose and glucose filled inside two holes of a polystyrene block have been identified. However, considering practical applications of THz-CT, we have to face a strong limitation which is the long acquisition time arising from use of THz time-domain spectroscopy. This is because THz-CT based on THz-Time Domain System needs serial scanning of four mechanical stages for time delay, two-dimensional (2D) sample position and sample rotation to record the series of THz projection images at multiple angles. In particular, the mechanical stage for time-delay scanning is the most time-consuming due to its reciprocating motion.

2. Data Processing and reconstruction

Tomography is an imaging technique used to reconstruct the volume of an object from a set of projections done from the exterior of the object. This technique is known since the beginning of 20th century with Johann Radon works.

Mathematically, the tomographic process is composed of two distinct steps. The first one describes the acquisition (direct model), i.e. how to get the measure set from the physical phenomenon (for instance, the beam attenuation). The second step defines the manner to reconstruct the volume from the acquired set (inverse model). Since these models are defined in continuous domain, they are not applicable directly and they have to be discretized. Moreover, the acquisition process is not reliable and undergoes artifacts altering the acquired data. Noise during the acquisition and approximations induced by the discretization generate errors on the reconstructed data. Consequently, one of the research areas in tomography during the last decades was to develop methods to reduce the discretization and noise errors in the reconstructed images.

2.1. Direct methods

We develop in this section the acquisition model based on the Radon transform. The inverse model giving the image modeling of the acquired object is detailed through the back projection of filtered projections. Direct reconstruction in the frequency domain is also explained. These models are defined in the continuous domain and have to be discretized to be applied in tomography. The discretization step, its limitations and main goals developed to minimize limitation effects, are the main drawbacks of these approaches.

2.2. From the physical phenomenon to the reconstruction

The rays used in tomography (for instance X-Rays, THz radiations, electrons) have an energy allowing them to go through matter. During this process, the ray beam undergoes attenuation proportional to the density of the traversed matter (which is not fulfilled in the reality for THz waves). It is for instance the basic principle for X-Ray radiography. In medical or industrial CT scanners, a 2D slice of the imaged object is acquired by casting rays following several angles around the object. For each angle, the attenuation of the ray beam is measured leading to a 1D projection of the object. A retro-projection method using the 1D set reconstructs the 2D slice modeling the acquired object [17].

Let's consider the following example with a 2D orthonormal and centered domain (on the left on Fig.4). Each 1D projection is defined along an angle θ . A projection line along θ depends on its position given by a module ρ . Such a line is denoted (θ, ρ) . The value depends on data traversed by the line and corresponds to the attenuation undergone by the rays into the matter along this line.

For a given angle θ , a set of modules and their values define the θ -projection-line, denoted R_θ (Fig.4a.). We denote S and we call sinogram the set of projections acquired around the object. The sinogram values are used to reconstruct the acquired domain with retro-projection. On the scheme on the right (Fig.4.b), the projection is retro-projected into the domain to reconstruct. One projection is not sufficient to recover the original domain. If the sinogram contains several projections (Fig.5a.), the original domain is reconstructed more accurately (Fig.5b.).

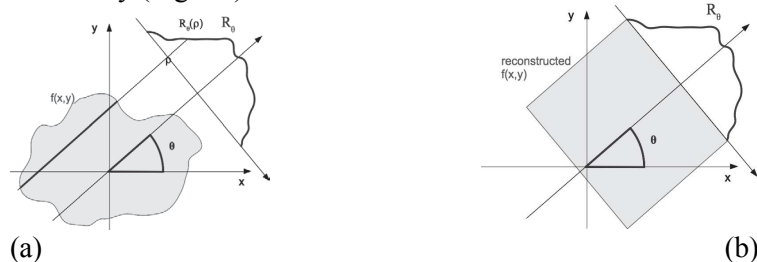


Figure 4: (a) A projection line is defined by an angle θ and a module ρ . (b) One projection is not sufficient to recover the original domain.

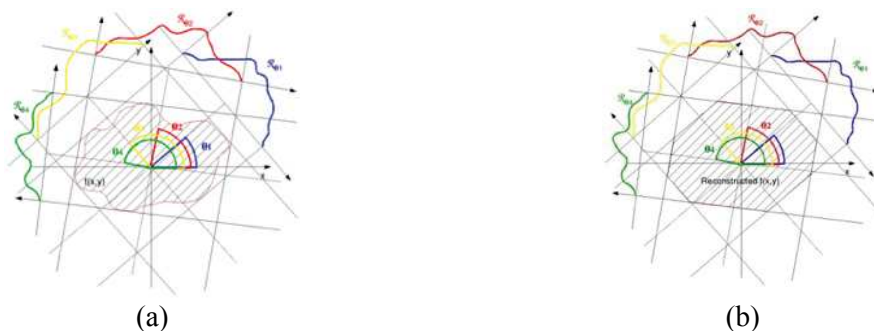


Figure:5 (a) Acquisition along several angles. (b) The intersection of data contained on the different projections allows reconstructing the original domain more accurately.

2.3. Acquisition properties

Contrary to an ideal acquisition, a real-condition acquisition is composed by a finite number of projections N_θ uniformly distributed between 0 and π . The module number denoted N_ρ is also finite and remains constant during all the acquisition. The angular step between two successive projections is $d\theta = \frac{\pi}{N_\theta}$. Similarly, we denote $d\rho$ the sampling step on the projections, i.e. the distance between two successive projection lines. During the discrete image reconstruction I , sized $W \times H$ pixels, the sampling step is $d\rho = \frac{MAX(W,H)}{N_\rho}$.

An acquisition with N_θ projections composed of samples gives the sinogram S^* , which is a sub-sinogram of the ideal sinogram S . It is represented by a 2D image, sized $N_\theta \times N_\rho$, where each line corresponds to the acquisition values of one projection. Supposing that i_θ and i_ρ are the projection and module indexes such as $0 \leq i_\theta < N_\theta$ and $0 \leq i_\rho < N_\rho$, the pixel (i_θ, i_ρ) contains the value, $R_{i_\theta}(\rho)$.

Let us consider a continuous model representing the Shepp-Logan phantom[18]. This model is based on an analytic definition of the objects defined in Fig.6 (a) represents this domain in an image sized 512×512 . An acquisition is done following 180 angles uniformly distributed between 0 and π , with 512 samples per projection. The resulting sinogram is given on Fig.6 (b). First line represents the 512 values of the 0° -projection, the second line contains the values of the 1° -projection and so on.

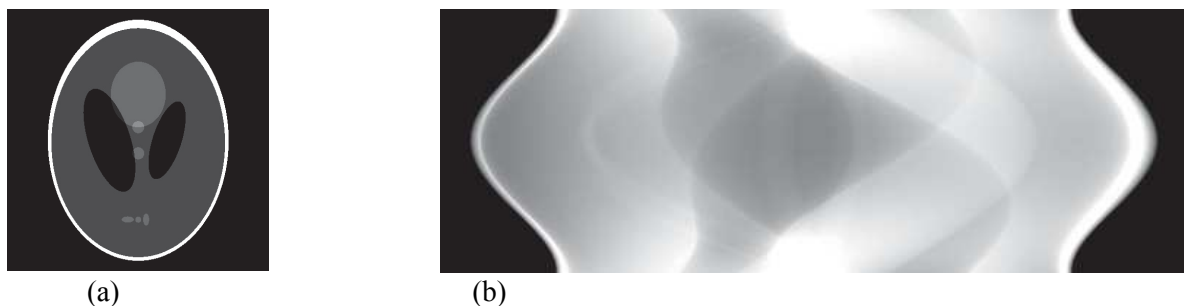


Figure 6 (a) Continuous Shepp-Logan phantom represented in an image sized 512×512 . (b) Acquired sinogram following 180 projections of 512 samples.

Such a sinogram can be used to reconstruct an image I modeling a layer of the acquired space (ex in fig.7). This one is performed using discrete versions of the Radon inversion or Fourier reconstruction.

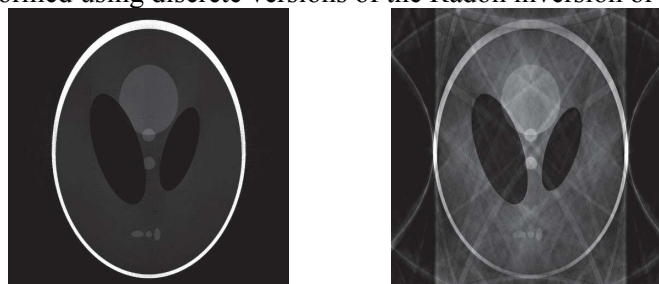


Figure 7: (a) slice of Sheep logan model (b) Reconstruction results from sinogram.

3. THz imaging in MetAMMI context

In the frame of the project, the THz imaging methods described above are used: TOF and THz-CT. This report refers to the task: A2.1.3. CNRS, with support from LNE, will measure the inner and outer geometry of polymer and ceramic implants and guides fabricated in A1.3.2 and A1.3.3 by THz-CT and

compare the results with the results achieved in A2.1.1. The results of this activity will be input in A3.3.2 in order to evaluate the metrological capabilities of THz-CT.

The materials under investigation were: For THz and X-Ray
 Ceramics: Silica, Alumina, Zirconia
 Polymers: PBS, ABS
 Metal (only for X-Ray)

3.1. Terahertz and X-ray reports: Two beams, two worlds

The objective of this section is to compare the performances and limitations of THz- and X-CTs based on the length measurement error test and probing error test described in the ISO 10360 series of standards. The steps of the measurement workflow are also considered.

The figure 8 displays these different steps leading from acquisition of projections sinogram to dimension extractions. It is important to emphasize that for X-ray tomography, numerous commercial software programs allow the reconstruction of 3D images which is not the case for terahertz tomography. The two main reasons are that this last technique is quite recent and that the physics of the interaction with matter is completely different with THz wave than with X-ray. For instance, the main reason is the huge difference between the wavelength and the dimension of the object. We face the same situation if you want to characterize a sphere of 10 nm diameter with X-rays.

So, for THz waves, CNRS has developed its own numerical procedure.

The X-ray workflow is presented on the left of fig. 8 whereas, on the right, are presented the two THz waves workflows used into the project depending on the material properties, the dimension of the samples and the targeted resolution. In red, we underline the special data processing CNRS developed for the project. More precisely, in orange, we describe the different step using Terahertz-CT and in blue, the time of flight tools which are similar to tools developed for ultra-sound waves, transform time and propagation information into the third dimension.

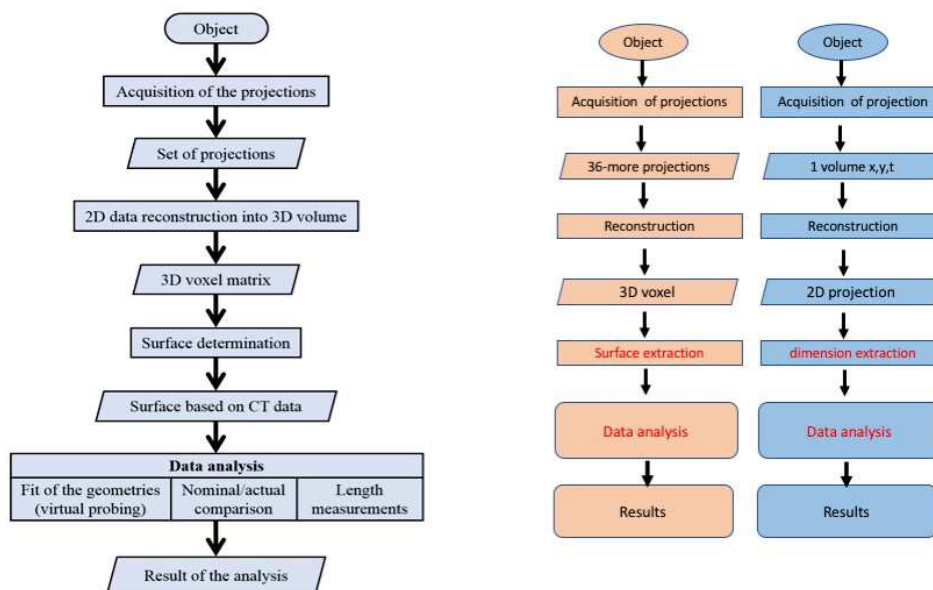


Figure 8: different workflows for X-Ray and THz-CT measurements.

3.2. Introduction to acceptance testing

During the purchasing process of a new measurement device, the decision to buy is primarily based on the technical specifications (i.e. the maximum permissible errors- MPEs). The MPEs of a coordinate measuring system (CMS) are obtained by a series of test measurements under specific conditions. Those test measurements and procedures are called acceptance testing. From the metrological point of view, acceptance testing creates trust in the measurement technology by helping to reach traceability to the metre (an SI unit) for the measurands under study, and by enabling fair comparability between different CMSs even over technology borders (i.e. featuring different sensors, for example X-ray CT and THz-CT).

A principle of acceptance testing is to assess the local and global error characteristics of a CMS. Local performance – showing the ability to precisely locate and measure the surface of a structure under test in a small spatial region – is assessed as a probing error test (*P*-test, Fig. 9 left) by means of measuring the size and form of a (small region of the measurement volume) test sphere. Global performance is assessed as a length measurement error test (*E*-test, Fig. 9 right) by means of measuring length reference standards embodying lengths up to the order of the dimensions of the measurement volume. Since acceptance tests are designed to test and to compare different measurement technologies, in this study, a length reference standard and a test sphere were measured by X-ray computed tomography and THz computed tomography and the measurement results as well as the whole measurement workflow were compared.

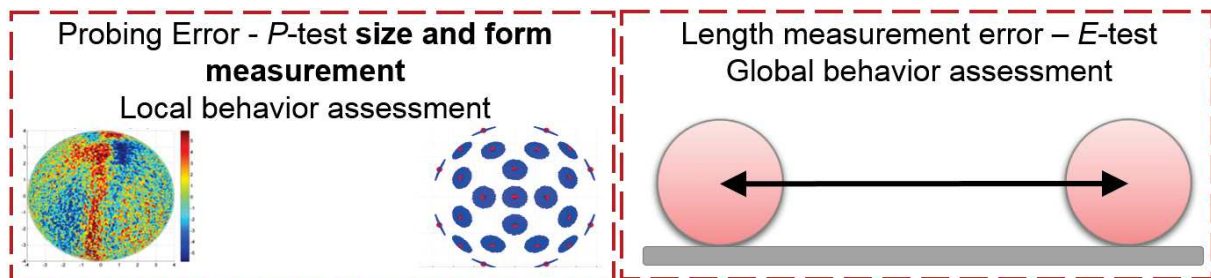


Figure 9: Description of the acceptance testing assessment: Probing error *P*-test of size and form of a test sphere, length measurement error *E*-test of a (long) reference standard.

- **Reference standards**

A polymer holed beak holder and a silicon nitride sphere (Figs. 10) were used to apply the acceptance test concept in the comparison. The polymer holed beak holder has size of 171 mm × 90 mm × 50 mm featuring holes of 8.5 mm, 10 mm, 18 mm and 30 mm in diameter. Although the holder is not considered suitable of being a metrological reference standard, it was used for this study due to its material and size, being more suitable for THz-CT measurements. Furthermore, the long-term stability of the beak holder is expected to be sufficient for the THz-CT measurements. On the other hand, for the probing test, the used silicon nitride (Si_3N_4) test sphere has 8 mm in diameter and form error below 0.3 μm . The sphere was calibrated at PTB using a high precision tactile micro coordinate measurement machine and it is attached in a carbon fibre shaft to facilitate the clamping for the measurements.

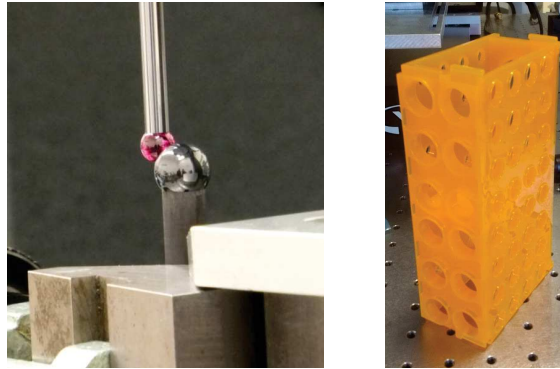


Figure 10: Standard objects used for the XCT and THz-CT comparison: silicon nitride sphere with 8 mm in diameter (left); polymer beak holder featuring different holes (right).

3.3. Experimental setups

3.3.1. X-ray CT scans

In metrological CTs, the workpiece rotates, usually using a high precision rotary table, and a lot of projections (i.e. radiographic images) are obtained from different angles of the objects.

The micro focus X-ray source used in this study is equipped with a reflection target made of tungsten with minimum focal spot size of approximately $3\ \mu\text{m}$. The XCT system is also equipped with a 2D flat panel detector featuring cesium iodine scintillators with 2000×2000 pixels with pixel size of $200\ \mu\text{m} \times 200\ \mu\text{m}$.

For XCTs, the most common configuration features a cone beam X-ray source, see Fig. 11. This means that the relative positions between the CT components (i.e. X-ray source, rotary table and flat panel detector) also have a large impact in the measurement results. When the reconstruction algorithm assumes for example a wrong position along z (see Fig. 11) of the rotary table relative to the X-ray source, scaling errors will be present, and consequently, length and size measurements will be significantly affected. To minimize this effect, in the used CT system a length measuring system is used to precisely determine the z -position of the components and the dependence between magnification and z -position is determined by the system calibration.

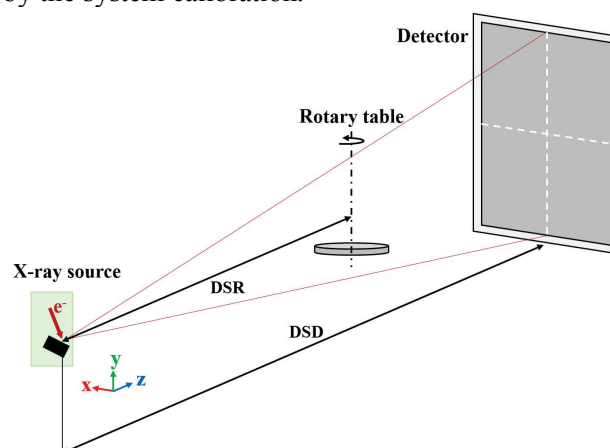


Figure 11: Cone-beam X-ray computed tomography set up; DSR is the distance source-rotary table and DSD is the distance source-detector.

Computed Tomography using X-rays (XCT) has long been used for industrial applications. XCT provides 2D X-ray images at different angles around the sample. All the internal and external geometries

are captured because X-rays pass through the sample. The reconstruction software calculates a 3D model from the 2D images. The surfaces of the measured object (e.g. STL-data) are determined from the 3D-model. From these data, e.g. dimensional characteristics such as size, position and shape can be measured.

For the XCT scans the beak holder was positioned vertically on the rotary table in the PTB's Nikon MCT 225 system. The Si₃N₄ sphere was positioned with the carbon fibre shaft parallel to the rotation axis of the rotary table.

The XCT scanning parameters are shown in Table 1.

	Beak holder	Si ₃ N ₄ Sphere
Voltage in kV	100	140
Current in μ A	190	110
Filter material and thickness in mm	-	0.1 mm Cu
Detector gain in dB	24	18
Magnification	2	17
Voxel size in μ m	100	11.5
Exposure time in ms	1000	2000
number of projections	1500	1500
Scan duration in min	25	50

Table 1. XCT scanning parameters used for the polymer beak holder and silicon nitride sphere.

3.3.2. THz-CT scans

“

For time of flight characterization, the experimental setup was a “TPS Spectra 3000” and a “TeraPulse 4000 systems “ from Teraview (Fig. 12). Basically, it uses a standard THz-TDS transmission setup based on a mode-locked Ti-Sapphire laser providing 80 fs pulses with a 76 MHz repetition rate. Typically, the useful bandwidth range of this instrument was between 0.1 and 4.5 THz, depending on the investigated sample under test. The laser output was split into pump and probe beams. The pump was focused onto a photo-switch for the generation of the THz field. This field was transmitted through the sample and was finally detected with a photo-switch triggered by the probe laser beam. Upon its interaction with the sample, the time-resolved field variation was measured using the variation in the photocurrent induced by the probe laser beam into the detector made of a LT-GaAs semiconductor. Finally, the photocurrent induced by the probe laser beam was filtered out and amplified. The time delay line allowed to sample the signal step by step and then to rebuild the THz field by sampling technique. In order to minimize noise effects, all the signals processed in this study correspond to the average of 50 acquisitions. The measurements were carried under dry air to remove water molecules absorption artifacts. A hygrometer controlled in real-time the relative humidity level, which was kept below 1% by using a flow of dry air. This control was performed in real-time through the monitoring of two spectral lines of water vapor at 1.12 and 1.7 THz, on the reference spectrum. The sample positioned at the focus point was located on a XY motorized stage.

The Teraview 3000 and TeraPulse 4000 systems provide TDS and spectral imaging in both transmission and reflection modes.



(a)



(b)

Figure 12: Photograph of (a) Teraview 3000 system, 1) Transmission mode and 2) Reflection mode, and (b) TeraPulse 4000 system, which is more compact and transportable.

In THz spectroscopy and imaging, broadband THz pulses are used to generate images and evaluate the optical properties of a sample from measurements made in both transmission and reflection modes. In THz imaging, measurements are taken on a 2D scan to generate a dataset of time domain waveforms [19]. In both the spectroscopy and imaging techniques, the pulses' time of flight produces depth information and fast Fourier transforms (FFT) are used to acquire spectral information. In general, the experimental setup for both THz systems uses transmission and reflection geometry, as shown in Fig. 12 (a) and (b), but only the transmission was used.

Teraview 3000 (Figure 12 (a)) illustrates the experimental setup for a THz transmission system, using photoswitches. The system properties are produced in the 0.2 - 3 THz frequency range, with a maximum density of 75 dB, a spectral resolution of 0.06 THz, and rapid scan mode (i.e. 30 scans/second). All measurements were made at room temperature, around 20 °C to 23 °C. One of the key considerations for image acquisition is the rate at which the THz waveforms are acquired, since this often determines the time required to form an image. Typically, spectral imaging is achieved by moving the (X,Y) translating stage with the terahertz beam focused on the sample position. A raster scan with a maximum area of 16×16 mm² is performed in the core chamber. Transmitted data for each pixel is acquired and converted from and to the frequency domain by FFT. Acquisition time ranged around from 10 min to 3 hours, depending on the scan parameters, including area of sample scanned and pixel size.

For the tomography acquisition, the setup is a 3D millimeter wave scanner composed of a millimeter wave source (Gunn diode coupled with a horn antenna) or a Frequency-modulated continuous-wave (FMCW) THz system. The former delivers an output power of 12 mW at 287 GHz. The THz beam is collimated and focused by a pair of Polytetrafluoroethylene (PTFE) lenses (focal length is $f = 50$ mm and diameter is $D = 50.8$ mm). The sample is positioned on a motorized stage comprising X,Y translations and a rotation around Z-Axis. Detection is performed by a Schottky diode, modulated at 1 kHz by a mechanical chopper. A lock-in amplifier (time-constant: 30 ms) acquires the transmitted THz signal intensity.

3.4. Data Evaluation

The data evaluation considers the most important steps present in the workflow of X-ray CT and THz-CT. It includes a visual-based comparison of the 2D images and the differences in the dimensional and geometrical analysis, if possible.

The dimensional and geometrical characteristics of the sphere, the diameter and form error covering at least at the equator line, excluding the shaft were calculated and compared between XCT and THz-CT measurements. For the beak holder, i.e. length measurement error, 6 center-to-center distances of the holes in the beak holder (Fig. 13) were measured and compared between XCT and THz-CT measurements. The center-to-center distances in the holes were defined to be circumferential lines in the center height of the holes.

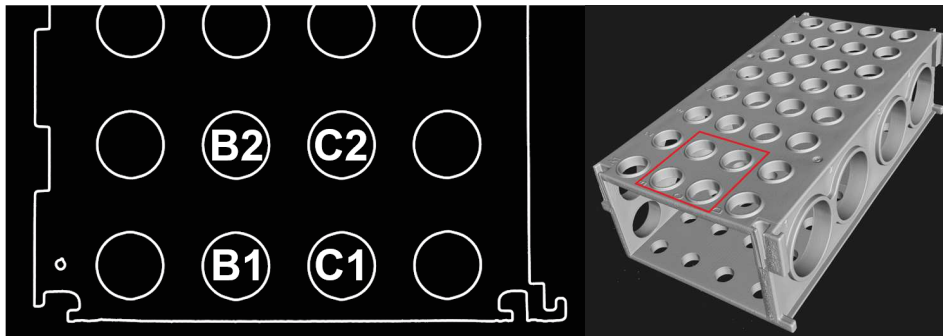


Figure 13: Description of the holes identification in the polymer beak holder used for comparison (schematic representation of the object).

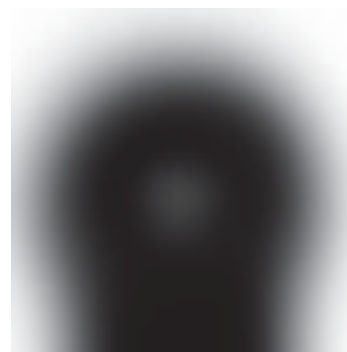
1. Results

- Visual assessment in the projections:

Already in the projections, significant differences between THz-CT and XCT can be observed. In the projection by THz-CT, it is possible to recognize the object which is being measured, e.g. the sphere and the beak holder, however with very low-resolution images causing unsharpness of the images with boundaries difficult to localize. In Fig 15 obtained at higher frequency, images with a better resolution and definition are obtained. XCT have clear and sharp images, see Fig. 14d due to the factor 100000 of the wavelength and the energy with respect to THz and the resolution of the sensor. We can also note the artefact in the center of the THz image (Fig. 14 (b)) due to focusing effect and the diffusion zone around the external diameter due to diffraction



(a)



(b)



Figure 14: a) X-Ray, b) 300 GHz picture of a nitride ball c) X-Ray projection, d) 300 GHz projection.

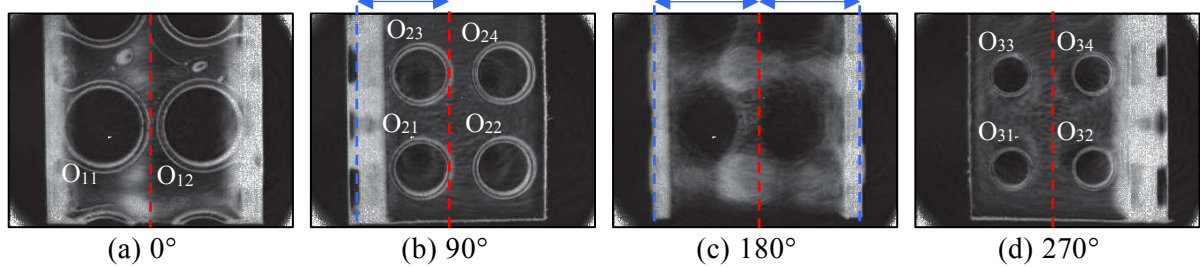
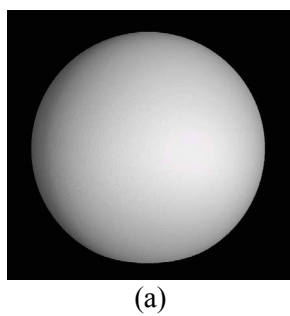


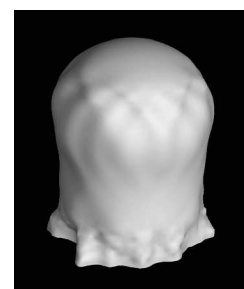
Figure 15: Absorbance projections at 2,5 THz on a scale of 0 to 30 dB according to four angles of view of the object obtained with the full field imager at 2.5 THz at (a) 0° (b) 90° (c) 180° (d) 270°

- Visual analysis in the reconstructed volumes:

The reconstruction of the 2D images into a 3D volume is the outcome of the projections. If the projections have good quality, the reconstruction will also have good quality. For the THz-CT reconstruction, it starts to be difficult to recognize the structure of the object being scanned, since at 300 GHz artefacts and diffraction inherent to propagation effect are the main part of the external surface [20](fig 16).



(a)



(b)



Figure 16: Visual comparison of the reconstructed volume (a) 8 mm sphere by XCT, (b) 8 mm sphere by THz-CT; (c) polymer beak holder reconstructed volume by XCT and (d) beak holder by THz-CT at 2.5 THz.

3.4.1. Dimensional and geometrical analyses

The Si_3N_4 8 mm in diameter sphere and the polymer beak holder were scanned with XCT and THz-CT. The diameter and the form of the sphere were calculated using the XCT data. The diameter and form of the sphere by XCT was calculated by a non-constrained least-square fit sphere. The diameter and the form of this sphere are 7.995 mm and 7.24 μm , respectively.

In the beak holder, the distances between the holes B1, B2, C1 and C2 were measured (Fig 17). With XCT, the distances are measured as a centre-to-centre length between two circles at specific height. Despite the good acquisition at 2.5 THz (fig 15), it was very difficult to properly measure the diameter and the form of the sphere using the THz-CT dataset.

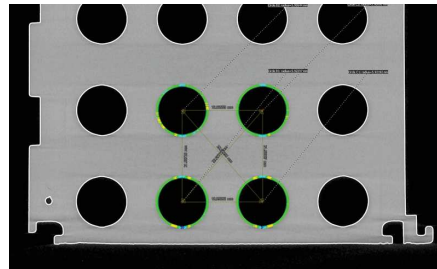


Figure 17: Centre-to-centre lengths measured in the polymer beak holder with XCT. Gray values represent the CT data, white contour represents the surface of the CT data, and green contour represents the data points used for the fitting of the circle.

Source A	Source B	XCT results in mm	THz-CT results
Circle B1	Circle B2	21,537	Not possible or very difficult
Circle B1	Circle C1	18,894	
Circle B1	Circle C2	28,650	
Circle B2	Circle C1	28,609	
Circle B2	Circle C2	18,836	
Circle C1	Circle C2	21,534	

At the moment, it was not possible to use THz-CT for measuring any distances using this approach .

3.5. Extraction of coordinates and diameters of circular openings on THz images

Due to the difficulty to correctly quantify the dimension with a 3D approach, we decided to focus on the capability of THz by selecting some of the acquired projections and quantify the possibility to perform measurement and dimensional analysis.

The ability to estimate the position of an object from an image obtained point by point may depend on both the radiation wavelength of the imaging system but also on the uncertainty of the optical intensity in the measurement chain. In this part we will propose an approach to extract, first, the coordinates of the center openings in an object and secondly, their diameter with a THz system.

To estimate the coordinates of these openings in an image, we'll use an iterative method based on circular Hough transform [21]. We chose this method for its ability to detect circular shapes despite the presence of noise and lighting large change in the image. It can be used to detect the presence of people on a photo or to automatically estimate the position of the center of the pupil of the eye. Finally, an estimate of the diameter of the circular object is also available with this algorithm. A second method of diameter evaluation involves measuring the positions of two edges of the opening with two adjustments by a function "error" changed. The evolution of the transmitted intensity, as the metal edge is moved in the focused Gaussian beam, can be modeled by the equation 1. This function corresponds to the integral of the optical intensity transmitted by the transparent portion depending on the position of the edge $T(x)$ displaced compared to the center of the Gaussian beam x_0 . When the edge is exactly in the center of the Gaussian beam and its position is found in the mark of the profile of the image at $x = x_0$:

$$T(x) = \frac{I(x)}{I(x_0)} = \frac{1}{2} \left(1 \pm \frac{2}{\sqrt{\pi}} \int_0^{\sqrt{2} \frac{(x-x_0)}{\omega_0}} e^{-t^2} dt \right) \quad (1)$$

The possible values of this function are between 0 and 1. With a profile adjustment by this equation, the knowledge of a prior on the parameters used to estimate the position of the edge and the size of the beam directly. However, phenomena such as reflection losses, interference between rays having taken different paths or Fabry Perot effect when the object is plane (which can induce a non-representative profile of the object) will be ignored.

3.6. 2D measurement from the point by point imaging

We will estimate the position of the centers and the diameter of several holes This part was obtained by a 3D printing in the polymeric material of ABS, widely used in additive manufacturing. Its radial dimension is $L * L = 50 * 50 \text{ mm}^2$, its thickness $d = 8 \text{ mm}$ and the through holes are 4 mm in diameter.

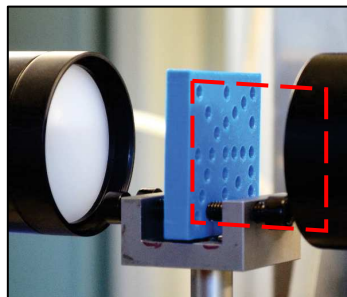
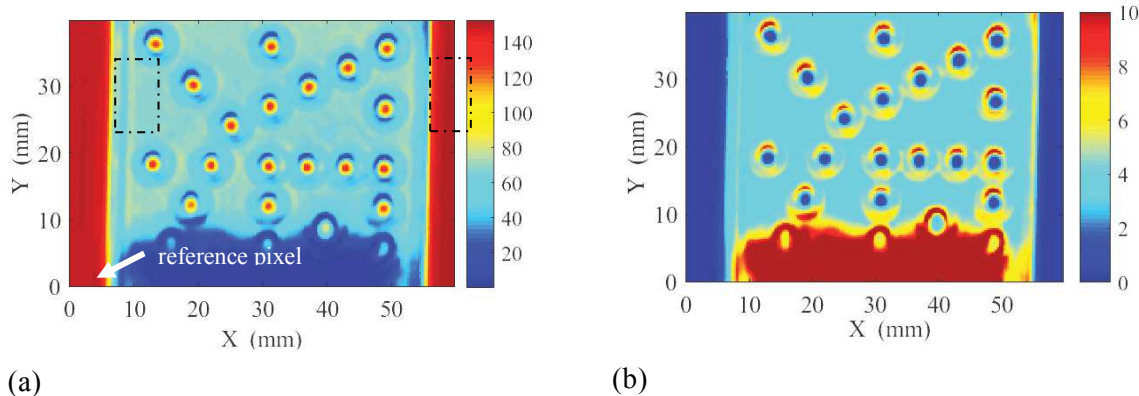


Figure 18: printed object during the point by point imaging at 0.287 THz.

The point by point imaging system is composed of a Gunn 0.287 THz source with a square horn, of four PTFE lenses of 50 mm diameter and of a Schottky detector with conical horn connected to a synchronous detection amplifier SR830. The focusing lenses on the object and collimation after crossing are both 50 mm focal length, and therefore with an $f/1$.

A picture of the object moving into the focused beam of the imager to 0.287 THz is shown in Fig. 19. The resulting image is comprised of 160 by 240 pixels and the pitch between two points is 0.25 mm. With an absorption coefficient of 0.97 cm^{-1} at 0.287 THz and a refractive index of 1.62, the expected absorbance after passing through the solid material was 3.9 dB.



(a) (b)
Figure 19: Images of the subject test at 0.287 THz: (a) transmission (b) absorbance in decibels.

In Fig. 19 the transmission image (a) and absorbance picture (b) are shown. Since the light is the same regardless of the pixel of the image point by point, the absorbance is calculated by taking as reference, the coordinate pixel (1,1) where the perturbation by the object on the focused beam radius of 1.9 mm can be considered negligible. It is noted that the absorbance image displays peaks of absorbance ($<10 \text{ dB}$) crescent-shaped around the holes. These can be explained by a part of the beam passing through the opening that interferes with another part of the beam passing through the object. Note also that all those croissants are located either on the top or on the bottom of the openings. This asymmetry may be due to a non-circular profile of the focused beam (elliptical). Despite these effects are not representative of the object, we will firstly assess the coordinates of the center openings and secondly, estimate their size through the adjustment described above.

An automatic estimate of the coordinates of the center of the 15 openings is performed by the Matlab function "imfindcircles" based on the Hough transform of circular, with the input parameters: the image transmission displays on Fig 19 (a), a minimum radius and a maximum radius. This method is very effective to find the coordinates of the corresponding pixel in the center of the circular object and their diameter. However, this method does not allow an estimate of more precise details as a digital resolution of 0.25 mm per pixel is used. In addition, for diameters of openings smaller than 10 pixels, the "imfindcircles" does not guarantee the accuracy of the estimate of the coordinates. In contrast, the measured intensity around the openings of the center can be used to adjust the coordinates of the centers by a Gaussian function in 2 dimensions. This adjustment is carried out on a square of $5 * 5 \text{ mm}^2$ around the center coordinates estimated by the circular Hough transform. The superposition of the transmission image of the aperture 8 and its Gaussian fit are shown in $r_{min} = 5 \text{ pixels}$ $r_{max} = 15 \text{ pixels}$ on Fig 20.

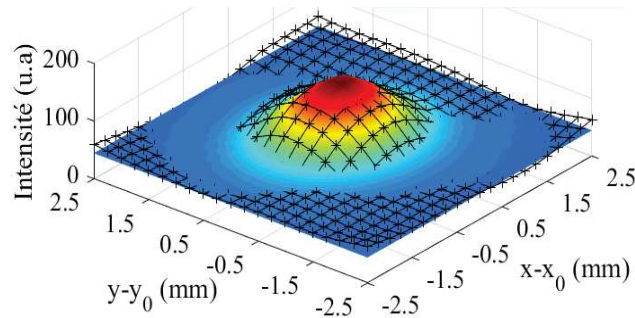


Figure 20 transmission of opening with its Gaussian fit

By repeating the operation on the 14 other selected openings, we could estimate the coordinates X and Y for each center with an uncertainty of less than 0.05 mm on the 95% confidence interval of the normal law (2σ). In the table 2, the distances between all the openings and opening No. 1 are compared with those of the model $\rho_{exp}\rho_m$. It is noted that the difference $\rho_{exp} - \rho_m$ between the center distance estimated by the Gaussian (fig. 20) fit and that provided by the 3D model of the piece of printing is less than 0.12 mm.

Openings No.	1	2	3	4	5	6	7	8	9	10
X	13,48	43.66	49.53	22.58	13.98	49,80	31.63	19.84	37.53	49.53
Y	18.75	33.29	27.16	18.51	36.65	36.10	36.62	30.55	18.22	17.93
ρ_{exp}	0	33.49	37,01	9.10	17.91	40.24	25.47	13.40	24.05	36.05
ρ_m	0	33.54	37.13	9.00	18,00	40.25	25.46	13.42	24.07	36.11
$\rho_{exp} - \rho_m$	0	0.05	0.12	-0.1	0.09	0.01	-0.01	0.02	0.02	0.06

Openings No.	11	12	13	14	15
X	43.4	31.63	25.75	31.42	37.76
Y	18.21	27.44	24.38	18.48	30.23
ρ_{exp}	29.92	20,12	13.50	17,94	26.85
ρ_m	30,02	20,12	13.51	18,00	26.84
$\rho_{exp} - \rho_m$	0.1	0	0.01	0.06	0.01

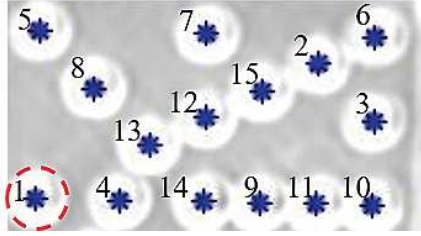


Table 2: Coordinates and distances (mm) from the center of the 15 openings estimated from terahertz imaging compared with the expected values.

Despite a wavelength of 1 mm and a discretization of 0.25 mm, scanning centers by the transformed circular Hough combined with the Gaussian adjustment allows an automatic evaluation of the distance between an opening with respect to another with a deviation from the model of 0.05 mm on average. It is from these two positions that the diameters of the openings along the axis X and Y are calculated. The average horizontal diameter calculated for all the apertures is 1.8 mm with a standard deviation of 0.1 mm and the mean vertical diameter of 2.0 +/- 0.2 mm or a through holes - 2 mm on the actual dimension. The adjustment by the error function allows an assessment of its width with a bias of only 0.03 mm. This method is not suitable when opening dimension is only 4 times the wavelength and / or when in a transparent material.

Measurement item		expected size	Criterion with error function	Minimum Criteria	Transform Circular Hough
Diameter openings (Average and standard deviation of 15 openings)	Horizontal	4	1.8 +/- 0.1	4.7 +/- 1.1	2.6 +/- 0.03
	Vertical		2.0 +/- 0.2	3.7 +/- 0.7	
Width of the object (average and standard deviation of 46 profiles) (mm)		50	49.82 +/- 0.03	46.83 +/- 0.12	-

Table 3: Average diameter estimation of the openings and of the width of the test object compared with the expected size.

This systematic bias of the determined diameters of the openings may have two explanations: the first lies in the diffraction limit of the imaging system; the object to be imaged is of dimension only 4 times the wavelength and the depth of field (2ZR) value of 4.6 mm is two times less than the thickness of the object. The other reason is due to multiple scattering on an edge that can induce interference, an unrepresentative transmission profile of the object.

One can measure the distance between two edges of the same transparent object, separated by a greater distance to eliminate the effects of proximity, and conclude on the origin of the bias. The positions X on both sides in all the profiles of the interval $Y = [21; 32.5]$ in the black box of the fig 21 (a) are determined by the Gaussian fit. We deduce an average width of 49.82 mm with a standard deviation of 0.03 mm for 47 profiles measured over the entire width, a bias with respect to the model - 0.18 mm. We finally found a consistent scale with the model.

To limit the effects of near one edge to the other, the frequency used can be increased to be imaged, and thus more accurately measure the dimensions of the openings. Four openings of the same object are imaged point by point, with the TPS 3000 (0.1 to 4 THz) in transmission with two translation stages X and Y. One of the outer surfaces of the object is positioned at the focal plane of the spectrometer. We present the acquisition of a timing signal over several points X and Y which can be used to image at a desired frequency after a FFT. In Fig 21, images of the amplitude of the FFT of a portion of the object on a square of $16 * 16 \text{ mm}^2$ are shown for four different frequencies. In Fig 21 (A), the background is grey because the material is transparent which is not the case at higher frequencies.

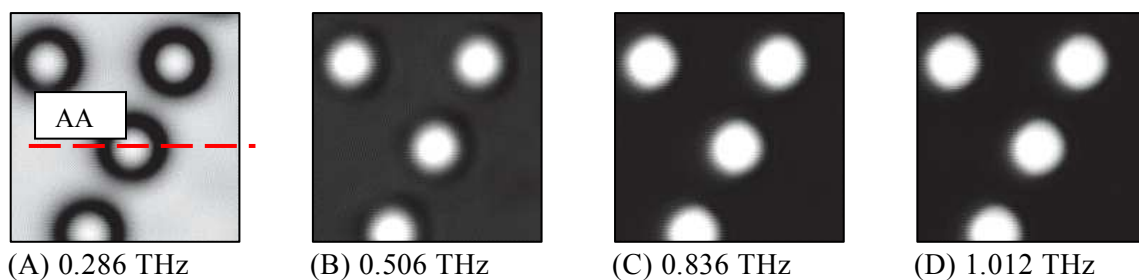


Figure 21: Image of four openings of the test object with four frequencies (0.286 THz; 0.506 THz; 0.846 THz; 1.012 THz).

A 0.286 and 0.506 THz, a decrease in the intensity at the edge of the openings is observed while at higher frequencies, in the transmission subject, it becomes negligible. Here we find the ring profiles that could be observed at 0.287 THz imaging with single frequency.

For the study, the term C-scan corresponds to an image according to the spatial dimensions X and Y for a given time, while a B-scan is a scan for a set Y (or X) in a spatial dimension (X or Y) and

the temporal dimension. In fig 22, the B-scan signal measured after passing through the object along the AA cut is presented in Fig 21. One can observe the lag time and the increase of the amplitude of the signal as the beam approaches the aperture whose center is estimated, in this reference, position $X = 8,5 \text{ mm}$.

We also represented four signals to coordinate points $X = \{0; 4.5; 6.5 \text{ and } 8.5 \text{ mm}\}$. One can observe the two pulses separated by 16.5 ps corresponding to the first at a crossing into the opening (AIR) and the second crossing in the object (ABS):

- $X_1 = 0 \text{ mm}$, the signal is composed of a single pulse for all the beam passes through the object thickness 8 mm.
- $X_4 = 8.5 \text{ mm}$, it is found that there is a maximum transmission at the center of the opening characterized by a pulse whose maximum amplitude is located at $t = 8.9 \text{ ps}$ in phase advance with respect to the signal $X = X_1$. In addition, a second low-frequency pulse can be observed whose maximum is located approximately at 11.5 ps and whose origin is a guided propagation in the opening. Finally, a third pulse synchronized with that $X = X_1$, shows a part of the beam has passed through the object.
- $X_3 = 6.5 \text{ mm}$, the center of the Gaussian beam profile is located at the theoretical left edge of the opening.
- $X_2 = 4.5 \text{ mm}$, the distance separating the center of the beam from the left edge of the opening is equal to the theoretical radius of the object. One can see the influence of the opening on the beam, by the appearance of a peak offset and synchronized with the main peak in $X = X_4$.

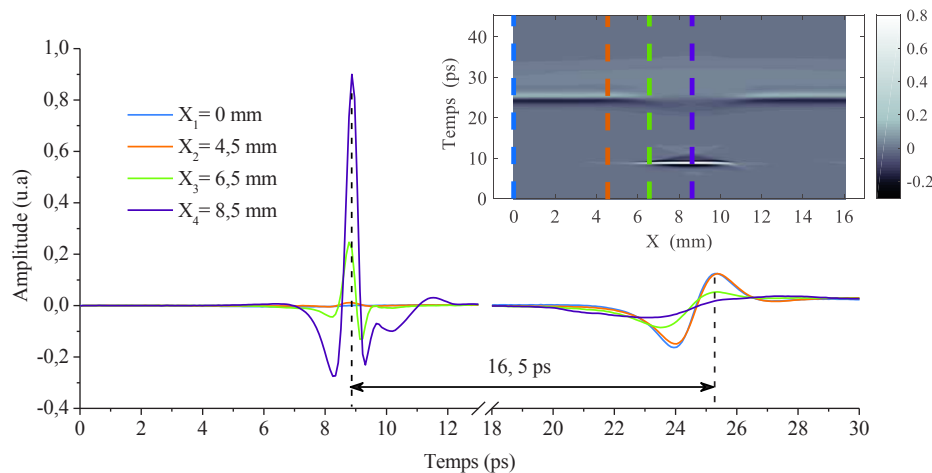


Figure 22: B-scan section AA and signal depending on the time at the four-coordinate points $X = \{0; 4.5; 6.5 \text{ and } 8.5 \text{ mm}\}$

Although there is a guided propagation of interface-ABS in the opening, we will propose a division of the signal with a portion of the beam through the object and another part not through the air. With consistent measure, we can separate the two pulses in time. Two FFTs are performed for each of the points of the profile; first considering only the measurements made on time and a second interval on, the rest of the signal is replaced by a zero amplitude (zeros padding) to keep the same frequency resolution of 22 GHz in both cases. In $T_1 = [0, 18] \text{ ps}$ and $T_2 = [18, 45] \text{ ps}$ on Fig 23, the amplitude of the FFT is plotted on a logarithmic scale as a function of frequency for the four positions X_1 to X_4 and considering each of the two intervals T_1 and T_2 separately. One can note the decrease of the signal as the frequency increases. Considering a noise level of 20 dB, we can see that the object is opaque beyond $F = 1 \text{ THz}$.

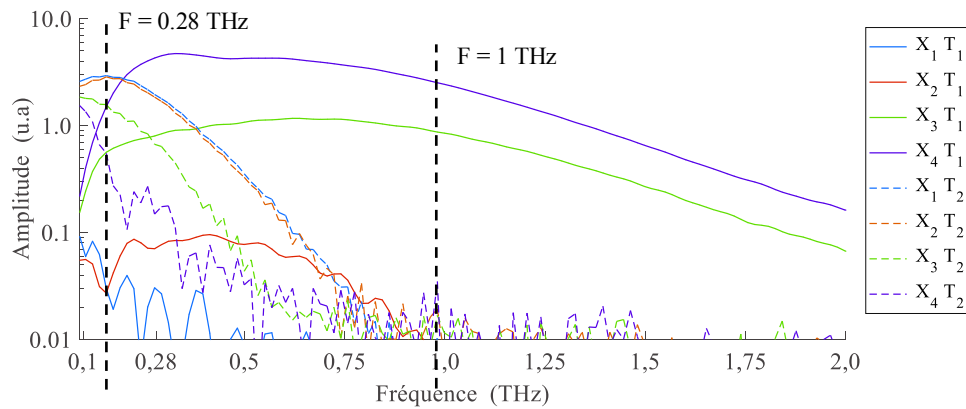


Figure 23: Modulus of the FFT according to the frequency of the radiation, calculated for the two time slots and four positions $X = \{0; 4.5; 6.5 \text{ and } 8.5 \text{ mm}\}$ $T_1 T_2$.

In contrast, for sub terahertz frequencies, there is much higher amplitude to the noise level after transmission through the object and in particular at a frequency of 0.28 THz to the X3 position. We can then expect interference when attempting to image with an incoherent detection in this position where the terahertz beam is "divided in two pieces" by the edge of the opening.

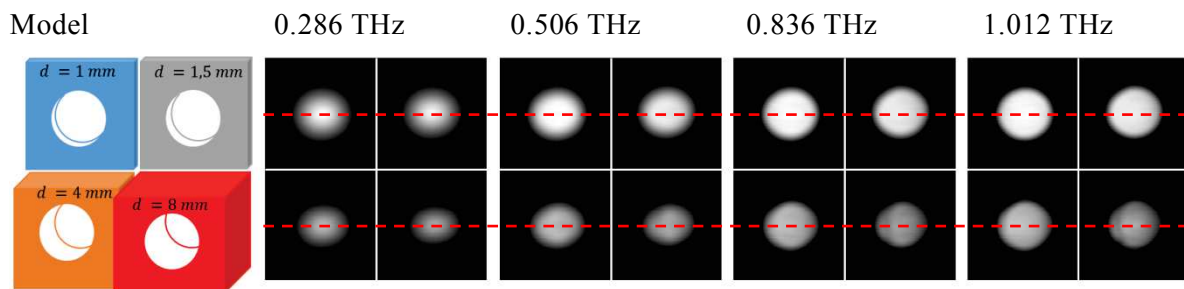


Figure 24: 4 metal blades Model thickness 1; 1.5; 4 and 8 mm, each having an aperture of 4 mm in diameter, and amplitude images calculated to 0.286; 0.506; 0.836 and 1.012 THz.

We can see the improvement of the quality of images as the frequency increases. However, there is a significant reduction in the diameter of the task when the thickness is 8 mm. We now estimate the diameter of the openings through the circular Hough transform and the fit with the error function.

In Fig 24, we have shown the horizontal profiles of the openings in thicknesses of 1 to 8 mm for the four frequencies as well as adjustments in each of the two edges. Determining is used to estimate the diameter with an uncertainty on the position of each of the two edges equal to the standard deviation $2x = x_0\sigma$ of the normal distribution (95% confidence). We note the increase in estimated diameter as the frequency increases and when the thickness is 1 mm. With the thickness of 8 mm on the other hand, we note that at 1.012 THz, it is only 3.76 mm, or 0.24 mm less than the expected thickness.

In addition, we note the general increase in uncertainty about the extent the thickness of 8 mm. This increase is synonymous with adjustment by the error function less suitable. To confirm the trend, we plotted the estimated diameter of the band from 0.3 to 3 THz for thicknesses 1, 4 and 8 mm (fig 25).



Figure 25: Estimation with adjustment by the error function of the diameter of the opening in the metal plate of thickness 1; 4 and 8 mm between 0.3 and 3 THz.

It is noted that the diameter of the opening in the thickness of 1 mm is overestimated by 0.8 mm, and that in the thickness of 4 mm, it is underestimated. In the thickness of 8 mm, there is a significant decrease in the estimated diameter from 3.8 mm to 0.82 THz to a minimum of 3.65 mm to 1.6 THz. Here we find the effect of the depth of field which decreases with frequency, contributes to underestimate the diameter of the opening.

For this study, we demonstrated the ability from THz imaging to evaluate the distance between the centers of the openings of 4 mm diameter of a transparent object of 8 mm from its image at 0.287 THz ($\lambda = 1$ mm). A numerical simulation approach allows a good appreciation of the positioning and dimensions of ABS objects. However, the adjustment by the error function results in a systematic bias, caused by the diffraction, of about 2 mm on the estimated diameter. In addition, despite a reduction in the wavelength up to 0.15 mm, a size 20 times smaller than the opening, the estimated diameter remains below 0.5 ± -0.05 mm from the actual diameter. This bias is related to optical resolution degraded outside the focal plane with a depth of field less than the thickness of the object.

These results demonstrate the ability to estimate, by the terahertz imaging in transmission, the position in 2D circular dimension λ openings 4, with a bias of only $\lambda / 10$ ($100\mu\text{m}$ for 300GHz) and an uncertainty of $\lambda / 20$ ($\sim 50\mu\text{m}$ for 300GHz). However, these initial results are validated in various configurations (materials, frequency, geometry) with a reproducibility study. We now estimate the position and diameter of circular objects in 3D space by drawing on existing approaches tomography X-ray.

3.7. 3D measurement from the imaging field

The objective is to evaluate the possibility of extracting the coordinates of circular openings and dimensions of an object from its 2D images and the 3D tomographic reconstruction, obtained with the imaging field at 2.5 THz. In Fig .26 is brought to the test subject in question made from an index $n = 1.52$ polyethylene and absorption coefficient 0.36 cm^{-1} at 2.5 THz, which can be divided into three subsets S1 in the foreground, S2 to the right of S1 and S3 back to S1, corresponding to the three faces of this parallelepiped object.

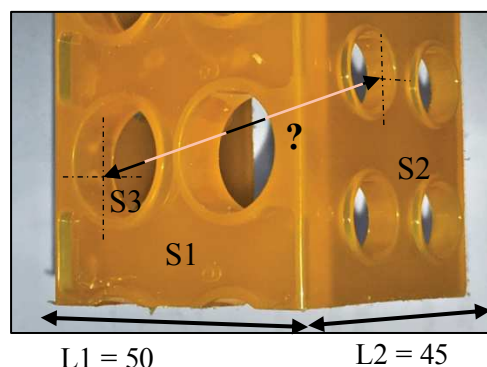


Figure 26: Picture of the polyethylene test object containing a plurality of apertures of different diameter on each of its three sub-assemblies S1, S2 and S3.

Each of these subsets contains circular openings of different diameters. The subassembly S1 includes two full apertures with an inside diameter of 17.8 mm while S2 and S3 each contain four apertures of diameters 11.8 mm and 8.4 mm for S2 to S3 and the centers of which are aligned together (Fig 26)

It can be seen firstly that the diameters of the apertures are much larger than the wavelength (100 μm) which theoretically provides good resolution at the focal plane, and secondly that the total width of the object is much greater than the depth of field of the lens (> 8 times greater), which does not provide a clear picture of the entire object on a single projection. It is also noted that, most absorbent portion of the object is located away from the geometric center (> 20 mm). To obtain the greatest possible details of the three subsets of the object, the latter is placed so that the outer surface of its subset # 1 is in the focal plane of the objective.

In Fig 27, the absorbance images on a scale of 0 to 30 dB for angles 0° , 90° , 180° and 270° are presented. A clear image can be observed for the projection 0° (a) to visualize the number "8" in relief on the outer surface of subset # 1 and defects. In addition, it is found that the object edges show a strong absorbance which is due to the refractive effects of beam deflection. One can also notice the change in absorbance due to a variation in thickness of about 1 mm on the subset # 1. Finally, one can observe on the projections 90° (b) and 270° (d) the influence of respective opposite subassemblies located more than 40 mm in the background, both by their misaligned openings which reveals the lower magnification off focal plane, but also by a disturbance of the overall lighting.

The center of rotation of the object, which is also the center of the image, was spotted on Fig 27 by a pin red. We spotted the pixel coordinates of the outer surfaces of the three parts of the object on the projections 90° and 180° from the center. We have: $\rho_1 = 107$ pixels; $\rho_2 = 118$ pixels; $\rho_3 = 122$ pixels

Finally, each of the openings is designated by the following nomenclature: The letter 'O' followed by the subset of the number of the corresponding object and a number of 1 to 4 (1-2 to subset # 1).

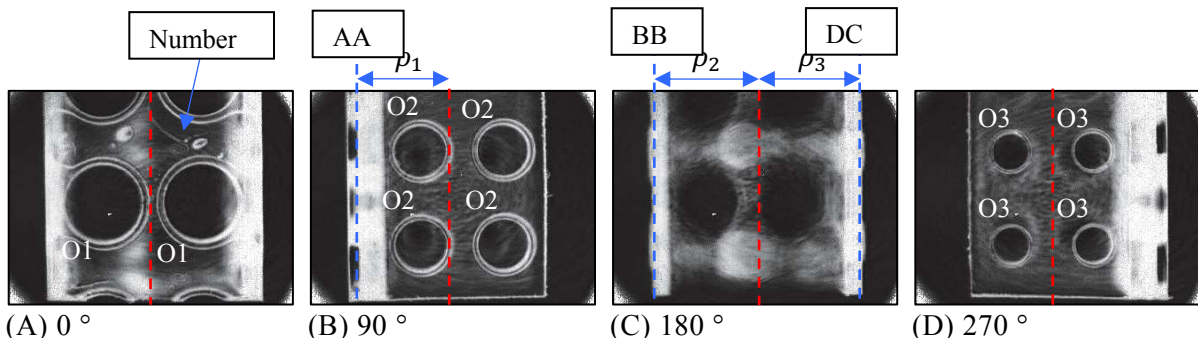


Figure 27: Absorbance in projections on a scale of 0 to 30 dB in four angles of the object obtained with the imaging field to 2.5 THz at (a) 0° (b) 90° (c) 180° (d) 270° .

From 360 screenings in transmission from 0° to 359° in 1° (XY θ volume of $320 * 240 * 360$ voxels), we conducted a tomography algorithm considering the Gaussian nature of the beam and the same parameters used for the reconstruction. The result is an XYZ volume of $320 * 240 * 320$ whose central axis, is located at the center $X = 160$ and $Z = 160$ along the axis. To attach a 3D landmark, the axis is selected as the normal to the surface of subset # 1 and the axis normal to that as subassemblies # 2 and # 3.

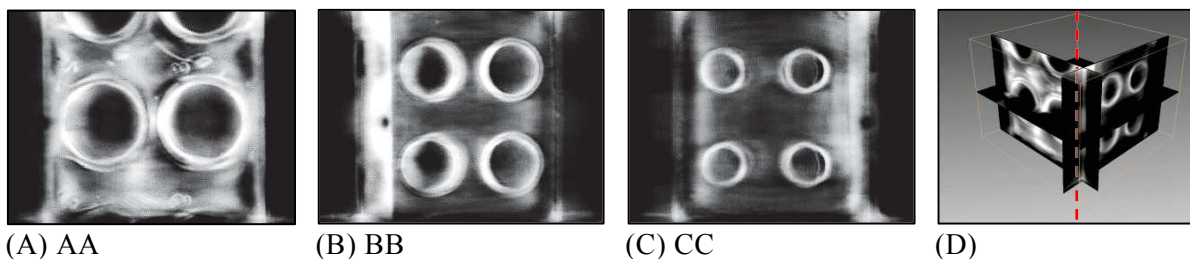


Figure 28: Cuts volume obtained by tomographic reconstruction of the test object according to (a) AA (b) BB (c) CC and (d) 3D visualization according to AA and BB cuts.

In Fig 28, AA, BB and CC sections and a 3D representation of the sections AA and BB of the result of tomography are presented on a scale of 8 bits 0 (black) to 255 (white) on the entire volume. The value 0 is assigned to the voxels of the volume corresponding to transparent material, the value 255 is in turn attributed to the voxels corresponding to the maximum calculated absorption coefficient. The maximum absorption coefficient calculated by the algorithm is 0.125 cm^{-1} , about 3 times less than the real coefficient of the object. Therefore, it is expected that the reconstruction contains artifacts with areas where the absorption coefficient is overestimated (areas in the air essentially).

We estimated the distance between the openings of the object as well as their diameter, from projections and 3D reconstruction shown in Fig 29. All coordinates X, Y and Z are indicated in pixels. The coordinates of the three projections corresponding to three subsets XS are calculated with respect to the rotation axis with positive values on the right. Regarding the X and Z coordinates of the reconstructed volume, reference is given in fig 29 (D) taking again as a reference the axis of rotation. For projections and cuts into the volume, the axis coordinates are calculated from the center axis which intersects the image (or the volume) into two equal parts with positive values up images. All distances are given in mm with an uncertainty of 0.2 mm since the magnification of $\frac{1}{4}$ of the lens to the object plane and the pitch of the framing sensor of 0.05 mm to the image plane.

The estimated coordinates of the center openings and the evaluation of their diameter are performed by the circular Hough transform for each of the openings with the input parameters: projections absorbance (or cuts in the 3D reconstruction), a radius minimum of 20 pixels (4 mm) and a maximum radius of 60 pixels (12 mm). In the table 4 are shown the position and estimated diameters of each of the openings. From these details, we were able to compare the estimated distances between the centers of openings compared to those measured in caliper, first on 2D projections taking the OS1 opening for each of the three subsets, then secondly on the three sections of the reconstructed 3D object by taking as reference the O11 opening for all other openings. It is noted that the distance between 2D and the distance between points in 3D on average undervalued with a relative difference of about 3%. In respect of diameter, we can notice that it is underestimated by an average of 0.7 mm from the projections overestimated and about 2.4 mm from the cuts in the volume.

Opening		O11	O12	O21	O22	O23	O24	O31	O32	O33	O34
Estimated coordinates of the center openings of the three projections (pixels)	X	-52	57	-37	56	-36	57	-53	37	-52	39
	Y	-5	-4	-52	-52	52	53	-52	-52	52	52
Estimated spacing in relation to the No. 1 of the corresponding subset OSS1 (+/- 0.2 mm)		0	21.8	0	18.6	20.9	28.1	0	18.1	20.7	27.8
Expected spacing (+/- 0.1 mm)		0	22.8	0	18.9	21.2	28.6	0	18.9	21.5	28.6
Gap (mm)		0	- 1.0	0	- 0.3	- 0.3	- 0.5	0	- 0.8	0.2	0.9
Relative error (%)		0	- 4.4	0	- 1.6	- 1.4	- 1.7	0	- 4.2	0.9	3
Estimated diameter (mm)		17.1	16.9	11.3	11.2	11.1	11.0	7.8	7.7	7.5	7.5
Diameter expected (+/- 0.05mm)		17,80	17.75	11.80	11.80	11.82	11,84	8.47	8.41	8.44	8.43
Gap (mm)		- 0.7	- 0.9	- 0.5	- 0.6	- 0.7	- 0.8	- 0.7	- 0.7	- 0.6	- 0.9
Relative gap (%)		- 4.0	- 5.1	- 4.2	- 5.0	- 5.9	- 6.7	- 8.3	- 8.3	- 7.1	- 10
Opening		O11	O12	O21	O22	O23	O24	O31	O32	O33	O34
Estimated coordinates	X	-55	58	118				-122			

of the center openings of the reconstructed volume (pixels)	Y	-8	-7	-52	-52	52	54	-55	-52	51	50
	Z	107		32	-55	32	-56	-53	39	-53	38
Distance between center estimated O11 with respect to the opening (mm)	0	22.5	38.8	48.3	39.6	49.1	35.9	21.1	36.6	22.4	
Distance between expected center (+/- 0.5 mm)	0	22.8	40.2	50.0	40.8	50.7	37.2	22.0	37.7	23.7	
Gap (mm)	0	- 0.3	- 2.4	- 1.7	- 1.2	- 1.6	- 1.3	- 0.9	- 1.1	- 1.3	
Relative gap (%)	0	- 1.3	- 5.6	- 3.4	- 2.9	- 3.2	- 3.5	- 4.1	- 2.9	- 5.5	
Estimated diameter (mm)	19.4	19.6	14.2	14.1	14.2	13.9	10.9	10.9	10.7	10.4	
Diameter expected (+/- 0.05 mm)	17,80	17.75	11.80	11.80	11.82	11,84	8.47	8.41	8.44	8.43	
Gap (mm)	1.6	1.85	2.4	2.3	2.4	2.1	2.4	2.5	2.3	2.0	
Relative error (%)	9.0	10	20	19	20	18	28	30	27	24	

Table 4: Estimated by the circular Hough transform and comparison with the measure caliper center distances and diameters of the openings in the three subsets of the object from its projections for 2D measurements, and from its tomographic reconstruction for 3D measurements.

With the results, we can conclude that the presence of reconstruction artifacts (induced by a variety of side effects such as reflection, refraction at interfaces, non-uniformity of illumination or the reduced depth of field), transform circular Hough is nevertheless adapted to determine the center to center position to measure 1D dimensions in a 2D drawing

3.8. Uncertainties on measuring the dimension of an object with THz waves

Uncertainty factor of the measurement on the terahertz image	Limiting factor
Numerical resolution	Number of pixels in the image
Optical resolution limited by diffraction	=> frequency
Imaging out of focus	Confocal parameter => numerical aperture
Interference and Fabry-Perot effect	Index and material thickness
Refraction at the air-sample interfaces	Shape of the object and material index
Signal to noise ratio	Absorption coefficient of the object, power of the source, the detector

4. Advantages / limitations of THz and X-ray imaging

THz imaging 👍 Advantages

- Chemical recognition possible
- Large panel of frequencies available
- Good imaging contrast for low dense materials
- Non-ionizing, safe for samples and users
-

👎 Limitations

- Resolution: depending on frequency; in the range of the wavelength : 1 mm for 300GHz , 100μ 3THz
- Limited depth of penetration, varying with material and frequency
- Monopixel detector: slow process (few cameras are efficient)
- Acquisition time
- Refraction, diffraction, absorption limitations

X-ray tomography 👍 Advantages

- Well known technique: The actual reference for metrology purposes
- Resolution (few micrometers), to compare with wavelength
- Transparent to all materials
- Clear visualization
-

👎 Limitations

- Prices
- Ionizing
- Specialized personal for X-ray manipulation

Conclusion

- THz-CT is not mature enough from technological aspect and a lot of work is necessary to perform 3D dimensioning (considering physical limitations).
- No precise lateral measurements were possible with THz-CT, only defect detection or density change.
- Measurements were possible with the 2D images obtained by THz waves. This is a real new result of the investigation. This is only conceivable with polymers and some ceramics, having thicknesses limited by the Rayleigh criterium. In that case, with multispectral analysis, center of holes could be localized with $\lambda / 10$ precision.
- Dimensioning would be sample (material and geometry) dependent which limits the potential use of THz to limited applications.

Considering the used wavelength, performing dimensional measurements from THz images is not accurate enough with respect to the real dimension and the end user requirements. Indeed, the spatial resolution of XCT images is higher than the spatial resolution of THz-CT images. However, as listed above, there can be several advantages using THz waves instead of X-Rays waves for non-metallic samples such as polymer and ceramic samples additively manufactured. The next step will be the development of THz camera [22] and data processing to open up this technology to industrial partners.

References

- [1] J. B. J. B. Perraud *et al.*, “Terahertz imaging and tomography as efficient instruments for testing polymer additive manufacturing objects,” *Appl. Opt.*, vol. 55, no. 13, pp. 3462–3467, 2016.
- [2] X. C. Zhang, “Terahertz wave imaging: horizons and hurdles,” *Phys. Med. Biol.*, vol. 47, no. 21, pp. 3667–3677, 2002.
- [3] M. Hangyo, M. Tani, and T. Nagashima, “Terahertz time-domain spectroscopy of solids: a review,” *Int. J. Infrared Millimeter Waves*, vol. 26, no. 12, pp. 1661–1690, 2005.
- [4] K. B. Cooper *et al.*, “Penetrating 3-D Imaging at 4-and 25-m Range Using a Submillimeter-Wave Radar,” *IEEE Trans. Microw. Theory Tech.*, vol. 56, no. 12, pp. 2771–2778, 2008.
- [5] A. J. Fitzgerald *et al.*, “Catalogue of human tissue optical properties at terahertz frequencies,” *J. Biol. Phys.*, vol. 29, no. 2–3, pp. 123–128, 2003.
- [6] T. W. Crowe, T. Globus, D. L. Woolard, and J. L. Hesler, “Terahertz sources and detectors and their application to biological sensing,” *Philos. Trans. R. Soc. London Ser. a-Mathematical Phys. Eng. Sci.*, vol. 362, no. 1815, pp. 365–374, 2004.
- [7] P. H. Siegel, “Terahertz technology,” *Microw. Theory Tech. IEEE Trans.*, vol. 50, no. 3, pp. 910–928, 2002.
- [8] C. D. Stoik, M. J. Bohn, and J. L. Blackshire, “Nondestructive evaluation of aircraft composites using transmissive terahertz time domain spectroscopy,” *Opt. Express*, vol. 16, no. 21, pp. 17039–17051, 2008.
- [9] H. Zhong *et al.*, “Nondestructive defect identification with terahertz time-of-flight tomography,” *IEEE Sensors J.*, vol. 5, no. 2, pp. 203–208, 2005.
- [10] K. Ajito and Y. Ueno, “THz chemical imaging for biological applications,” *IEEE Trans. Terahertz Sci. Technol.*, vol. 1, no. 1, pp. 293–300, 2011.
- [11] S. Wietzke *et al.*, “Industrial applications of THz systems,” p. 738506, 2009.
- [12] V. P. Wallace, E. MacPherson, J. A. Zeitler, and C. Reid, “Three-dimensional imaging of optically opaque materials using nonionizing terahertz radiation,” *J. Opt. Soc. Am. a-Optics Image Sci. Vis.*, vol. 25, no. 12, pp. 3120–3133, 2008.
- [13] J. Takayanagi *et al.*, “High-resolution time-of-flight terahertz tomography using a femtosecond fiber laser,” *Opt. Express*, vol. 17, no. 9, pp. 7549–7555, 2009.
- [14] D. M. Mittleman, R. H. Jacobsen, and M. C. Nuss, “T-ray imaging,” *IEEE J. Sel. Top. Quantum Electron.*, vol. 2, no. 3, p. 679, 1996.
- [15] J. Radon, “Über die Bestimmung von Funktionen durch ihre Integralwerte langs gewisser Mannigfaltigkeiten.” *Ber. Ver. Sachs. Akad. Wiss. Leipzig*, in German. An english translation can be found in S. R. Deans : *The Radon Transform and Some of Its Applications.*, ” *Math-Phys. Kl.*, vol. 69, pp. 262–277, April, 1917.
- [16] A. Brahm, M. Kunz, S. Riehemann, G. Notni, A. Tünnermann, and A. Tuennermann, “Volumetric spectral analysis of materials using terahertz-tomography techniques,” *Appl. Phys. B Lasers Opt.*, vol. 100, no. 1, pp. 151–158, 2010.
- [17] A. Kuba and G. T. Hermann, “Discrete Tomography: Foundations, Algorithms and Applications.” Birkhauser, 1999.
- [18] L. A. Shepp and B. F. Logan, “The Fourier reconstruction of a head section,” *IEEE Trans. Nucl. Sci.*, vol. 21, no. 3, pp. 21–43, 1974.
- [19] J. P. Guillet *et al.*, “Review of Terahertz Tomography Techniques,” *J. Infrared, Millimeter, Terahertz Waves*, vol. 35, no. 4, pp. 0–30, 2014.
- [20] E. Abraham, A. Younus, C. Aguerre, P. Desbarats, and P. Mounaix, “Consideration of refraction losses for time-domain terahertz computed tomography,” in *Infrared Millimeter and Terahertz Waves (IRMMW-THz), 2010 35th International Conference on*, 2010, pp. 1–2.
- [21] T. J. Atherton and D. J. Kerbyson, “Size invariant circle detection,” *Image Vis. Comput.*, vol. 17, no. 11, pp. 795–803, 1999.
- [22] J.-B. Perraud, J.-P. Guillet, O. Redon, M. Hamdi, F. Simoens, and P. Mounaix, “Shape-from-focus for real-time terahertz 3D imaging,” *Opt. Lett.*, vol. 44, no. 3, p. 483, 2019.